Color-coded optical profilometry with $>10^6$ resolved depth steps

Erez Hasman and Vladimir Kleiner

A novel, to our knowledge, approach to light-stripe triangulation configuration that allows for parallel, fast, real-time three-dimensional surface topography with an extremely large number of optically resolved depth steps is presented, analyzed, and experimentally demonstrated. The method is based on a color-coding and decoding arrangement that exploits polychromatic illumination and axially dispersing optical elements. This leads to an increase of the depth-measuring range without any decrease in the axial or the lateral resolution. Our experiments yield three-dimensional surface measurements with lateral and depth optical resolutions of <40 nm, for a depth of focus of 48 mm, resulting in 1.2×10^6 resolving depth steps. © 2001 Optical Society of America

OCIS codes: 120.3940, 120.4630, 120.6650, 150.6910, 180.6900, 050.1970.

1. Introduction

Optical three-dimensional (3-D) profilometry measuring is essential for many fields in science and industry, observation of micro-optoelectromechanical systems, machined parts, integrated circuits, and biologic specimens.[1–3] There are a variety of electro-optical measuring approaches available for three-dimensional analysis of structures in the macroscopic range as well as in the microscopic. However, the structured light-triangulation method is the most widespread for shape measurement of a diffusing surface.[4] It is suitable for scientific and industrial applications in that it offers a simple and robust 3-D measurement. The simplest structured light system projects a single point of light from the source onto an object. The point is then imaged with off-axis configuration, on a lateral effect photodiodes or linear arrays of detectors. The single point triangulation approach is relatively inexpensive and has a high resolution. However, measuring the surface of 3-D objects involves lengthy time-consuming scanning, which is often impractical. A more complicated structured light system operates by projecting a light stripe onto the object and using a two-dimensional detector array for simultaneous measurement of a linear cross section.[5] Fewer frames are then required for measuring the entire 3-D object, and scanning need be done only in the direction perpendicular to the stripe.

Unfortunately, the conventional structured light-triangulation approaches, described above, cannot simultaneously achieve a large depth measuring range and a high lateral resolution. This is because the conventional optical lenses that are incorporated in these systems cannot, at the same time, provide both long focal depth and high lateral resolution. Specifically, high lateral resolution requires high numerical apertures, whereas large depth of focus requires low numerical apertures. The relation between the lateral resolution $1/\Delta x$ (Δx is the spot size) and the depth of focus δF is given by

$$\delta F = \kappa(\Delta x)^2/\lambda_0, \tag{1}$$

where λ_0 is the wavelength of the light and κ is a constant number between 1 and 6 depending on the exact definitions of Δx and δF and on the wave-front apodization.

A common trade-off between the lateral resolution and the depth of focus is to reduce the lateral resolution, i.e., to use a relatively large spot, the center of which can be determined with much higher accuracy than the spot size, by complicated numerical techniques.[6] Such techniques can overcome, somewhat, the errors that are due to the statistical noises, such as shot noise, CCD amplifier noise, CCD pixel re-

The authors are with the Optical Engineering Laboratory, Faculty of Mechanical Engineering, Technion-Israel Institute of Technology, Haifa 32000, Israel. E. Hasman's e-mail address is mehasman@tx.technion.ac.il.

Received 30 March 2000; revised manuscript received 2 January 2001.

0003-6935/01/101609-08$15.00/0

sponse nonuniformity, and quantization noise. Unfortunately, this approach is highly sensitive to systematic noises such as local changes in the reflectivity or the shape of the object (e.g., short radius of curvatures cannot be adequately dealt with). Moreover, for coherent illumination, speckle noise severely limits the possibility of achieving subspot size resolution.[7–9] An alternative approach, applicable to the single-point triangulation approach, is to use aspherical optical elements with a high resolution and long focal depth such as Axicon[10,11] or Axilens.[12] Unfortunately, these approaches cannot be directly adopted to the light-stripe configuration. Specifically, using such aspherical optical elements to form a light stripe with high lateral resolution and long focal depth will result in high side lobes; consequently, the peak-to-background ratio is relatively low.[13]

Recently, we presented what to our knowledge is a novel approach for extending the focal depth of light-stripe triangulation, using the color-coded approach in which these limitations were largely reduced and good peak-to-background ratios were obtained.[14] Although 18-fold improvement of the focal depth was demonstrated, the overall depth resolution was limited by detector noise and lack of sophisticated image processing to >10 μm, and the number of resolving depth steps (NRD) was a few thousand.

In this paper we present a comprehensive theoretical and experimental investigation of 3-D optical profilometry with light-stripe triangulation based on color coding and decoding that permits parallel, fast, real-time 3-D surface mapping with a large depth measuring range as well as high axial and lateral resolutions. The method is based on a color-coded arrangement that exploits polychromatic illumination and a cylindrical element that axially (longitudinally) disperses the incident light in order to increase the depth measuring range without any decrease in the vertical and horizontal resolution. We use an on-axis cylindrical diffractive optical element (DOE) and a combined diffractive–refractive optical element, whereby many light stripes, each of a different wavelength, are simultaneously focused at different focal lengths, forming a rainbow light sheet.

We investigate two main configurations. In the first configuration the rainbow light sheet is used directly to obtain the surface profiles. Here the increase in the focal depth is accompanied by a reduction in the peak-to-background ratio (although at a much smaller amount than the monochromatic configurations). In the second approach, color decoding is added by means of a variable-wavelength filter (VWF) whose dispersion is exactly matched to that of the rainbow light sheet. Both our theoretical analysis and our experimental results reveal that, with optimal decoding, the diffraction-limited spot size and shape are completely maintained even for a large increase in the depth of focus. Finally, low noise detection and sophisticated digital signal postprocessing are used to obtain <40-nm depth resolution, yielding $>10^6$ of resolving depth steps over the entire focal depth.

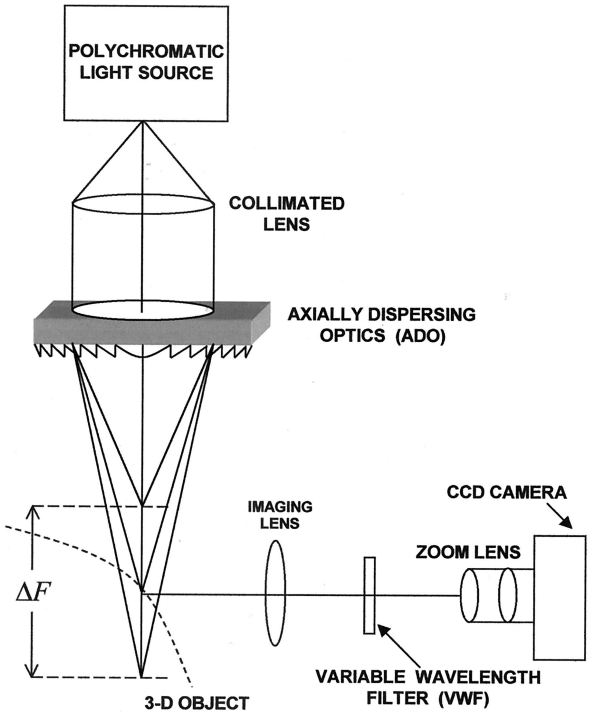

Fig. 1. Color-coded light-stripe triangulation system.

2. Basic Principle of the Measuring System

The operation of our color-coded light-stripe triangulation system is described with the aid of Fig. 1. The broadband light source (multicolor) can be either a white-light source or a short-pulsed laser that produces a relatively large spectral bandwidth. A collimating lens system forms plane waves that are focused by axially dispersing optics (ADO) such as a cylindrical DOE or a hybrid/combined diffractive–refractive optical element. The ADO forms a rainbow light sheet that consists of light stripes of different wavelengths (color) at different distances from the lens. An object with maximum height difference smaller than the rainbow focal depth ΔF is placed in the region of the rainbow light sheet. The object intersects the rainbow light sheet, and the intersection profile of the object is then imaged with an off-axis configuration (at an angle θ from the illumination optical axis) to a two-dimensional CCD camera. Although the rainbow light sheet is composed of thin stripes (limited by the diffraction) of the individually focused wavelengths, each stripe is surrounded by background light of other wavelengths. Thus the detected profile is relatively broad. This profile can be significantly narrowed by means of suppressing the background light and allowing the light of only the proper (focused) wavelength to be detected at each object depth. This is achieved by insertion of an interference filter into the detection path whose transmitted wavelength is spatially nonuniform. With such a VWF, optimal performance is

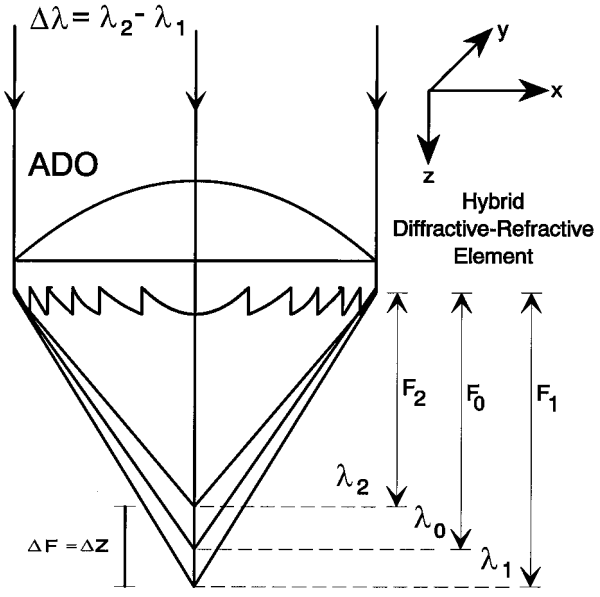

Fig. 2. ADO; hybrid diffractive–refractive optical element.

obtained when the spread and specific wavelength location matches that of the light from the axially dispersing optics. When the match is exact, it is possible to obtain a diffraction-limited resolution over the entire depth of focus without any scanning. The data that are detected by the CCD camera are displayed on a monitor and processed by the computer to give the intersection profile in virtually real time. After a line is detected, a computer-controlled stepper motor shifts the object to get another line, and so on, until a complete 3-D profile of the object is obtained.

We can evaluate the color-coded triangulation approach by resorting to a simple geometrical analysis and to physical optics considerations. The axially dispersing optics can be an on-axis cylindrical DOE or a hybrid combination of diffractive–refractive lens. Figure 2 illustrates a hybrid lens that is illuminated with a broadband light beam. The hybrid lens includes a plano–convex cylindrical lens with a diffractive element that has blazed grooves (kinoform) on the planar surface. The hybrid lens serves to focus on light stripes of different wavelengths at different distances from the lens. For example, the wavelength λ_1 is focused to the focal length of F_1, λ_0 is focused to F_0, and λ_2 is focused to F_2. For an idealized one-dimensional quadratic cylindrical DOE, the transmission function $t(x)$ is given by

$$t(x) = \exp[i\phi(x)] = \exp\left(-i\,\frac{\pi x^2}{\lambda_0 f_0}\right), \tag{2}$$

where x is the lateral coordinate in the thin DOE, ϕ is the phase function, and f_0 is the focal length of the DOE for a wavelength λ_0. When such DOE is illuminated with another wavelength λ, the resulting focal length $f_d(\lambda)$ is given by

$$f_d(\lambda) = f_0\lambda_0/\lambda\,. \tag{3}$$

Equation (3) indicates that the focal length is inversely proportional to the wavelength, which is the axial dispersion of the quadratic DOE. By use of a DOE with the quadratic phase function, it is possible to obtain the range of the rainbow light sheet (depth of measuring range) by the relation

$$\Delta F = \Delta z = f_0(\Delta\lambda/\lambda_o), \tag{4}$$

where $\Delta\lambda = \lambda_2 - \lambda_1$ is the illuminated wavelength band (λ_2 and λ_1 are the upper and the lower wavelengths, respectively) and $\lambda_0 = (\lambda_2\lambda_1)^{1/2}$. To match the dispersion of the ADO to a commercially available VWF or to change the depth measuring range ΔF while keeping the same effective focal length, it may be necessary to combine diffractive and refractive elements. In such a hybrid combination, the refractive lens has a focal length $f_r(\lambda)$ and the DOE has a focal length $f_d(\lambda)$ yielding an effective focal length $F(\lambda)$. A simple expression for the focal depth of the hybrid element can be approximated, assuming negligible separation between the refractive and the diffractive elements, and neglecting the dispersion of the refractive lens, as follows,

$$\Delta F \cong \left(\frac{F_0}{f_0}\right)\left(F_0\,\frac{\Delta\lambda}{\lambda_0}\right), \tag{5}$$

where $\lambda_0 = (\lambda_2\lambda_1)^{1/2}$ [assuming $\lambda_0 \cong (\lambda_2 + \lambda_1)/2$], $F_0 = F(\lambda = \lambda_0)$ and $f_0 = f_d(\lambda = \lambda_0)$. The enlarging factor of the focal depth M_o is defined as the ratio between the extended focal depth of the hybrid diffractive–refractive element, given by relation (5) and the monochromatic focal depth, $\delta F = 4\lambda_0 F_{\#}^{\,2}$ (80% of the maximal intensity), where $F_{\#}$ is the f-number of the hybrid lens. With this definition we get

$$M_o = \frac{\Delta F}{\delta F} \cong \left(\frac{\Delta\lambda}{\lambda_0}\right)\left(\frac{D^2}{4\lambda_0 f_0}\right) = \left(\frac{\Delta\lambda}{\lambda_0}\right) N^{\mathrm{DOE}}, \tag{6}$$

where D is the aperture diameter of the ADO and N^{DOE} is the Fresnel number of the diffractive element. N^{DOE} is also the axial resolving power of the ADO, i.e.,

$$N^{\mathrm{DOE}} \cong \frac{\lambda_0}{\delta\lambda_{\mathrm{DL}}}, \tag{7}$$

where $\delta\lambda_{\mathrm{DL}}$ is the wavelength range that maintains a diffraction-limited spot. Equation (6) indicates that the enlarging factor of the focal depth depends only on the Fresnel number of the DOE and on the illuminated spectrum band.

To obtain high axial and lateral resolutions in the measuring process, the rainbow light sheet is observed through a VWF, whereby the wavelength-transmittance function along the length of the filter exactly matches the axial dispersion of the ADO. In addition to completely restoring the diffraction-limited spot size, we should set a the filter transmittance bandwidth $\delta\lambda_f$ equal to (or smaller than) $\delta\lambda_{\mathrm{DL}}$ of relation (7). Defining the VWF discrimination M_f as

the number of the wavelength that can be discriminated, i.e.,

$$M_f = \frac{\Delta\lambda}{\delta\lambda_f}, \tag{8}$$

and using relations (6) and (7) yields the expected optimal filter discrimination as $M_f^{\text{opt}} \cong M_o$. As we show below, using VWF with such optimal M_f indeed yields a sharp image of the object profile with diffraction-limited and low sidebands. A commercially available VWF is a linearly variable interference filter, so it is desirable to obtain ADO with linear axially dispersion. This can be obtained with excellent accuracy in the limit $f_0 \gg f_r$.

From geometrical consideration, the resolvable depth of the system is given by

$$\delta z = \frac{\delta x_{\text{img}}}{\sin\theta}, \tag{9}$$

where δx_{img} is the resolvable lateral shift of the imaged light stripe (the center) on the CCD. In general, the resolvable lateral shift of the light stripe is proportional to the imaged stripewidth itself, where the proportional constant depends on the accuracy needed to determine the center of the image light distribution. A commonly used merit function to characterize the performance of the color-coded optical profilometer is the NRD as

$$\text{NRD} = \frac{\Delta F}{\delta z} = M_o \frac{\delta F}{\delta z}. \tag{10}$$

Equation (10) indicates that, for our color-coded system, the NRD can be increased by the factor of M_o, compared with the conventional monochromatic light-stripe triangulation, while maintaining the same lateral resolution.

3. Realization and Experimental Results

An automated 3-D optical profilometer was designed, realized, and evaluated experimentally and theoretically for the acquisition and measurement of 3-D surfaces. For the illumination source we used a continuous-spectrum 75-W xenon arc lamp of spectrum $\lambda = 0.4-0.7$ μm and used a heat-absorbing glass to reduce the IR radiation. The light emerging from the lamp is focused by a parabolic mirror onto a slit with a 15-μm diameter. The slit is imaged with a 4-*f* system. The first lens in the 4-*f* system is an achromatic lens with 360-mm focal length, and the second lens is the ADO, a combination of a cylindrical refractive lens designed to have $f_r = 496$ mm at $\lambda_0 = 0.529$ μm and a quadratic diffractive element, whereas the phase function is given by Eq. (2) and $f_0 = f_d(\lambda_0 = 0.529\ \mu\text{m}) = 1040$ mm. The gap between the cylindrical refractive lens and the diffractive element is 17 mm, owing to practical constraints. The aperture diameter of the combined lens is $D = 9$ mm. The diffractive element was realized with photolithographic techniques and reactive ion etching to produce a 16-binary-level element on a fused-silica substrate.[15]

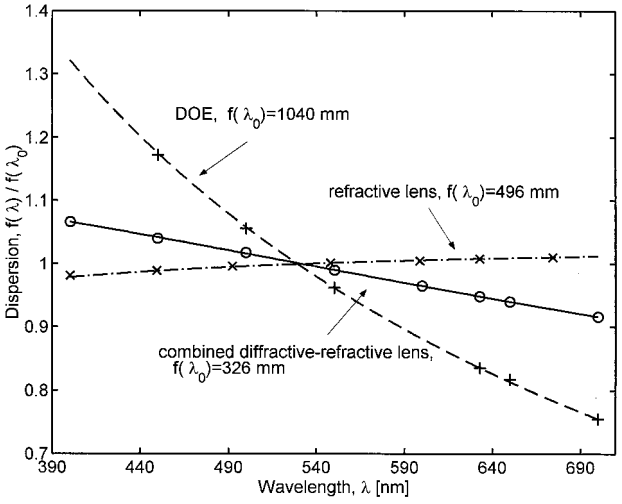

Fig. 3. Measured and calculated dispersion of the cylindrical lenses ($\lambda_0 = 529$ nm); refractive lens, measured (crosses) and calculated (dotted–dashed curve); diffractive lens, measured (pluses) and calculated (dashed curve); combined diffractive–refractive lens, measured (circles) and calculated (solid curve).

The measured and the calculated dispersion results for the cylindrical refractive lens and DOE separately and combined are shown in Fig. 3. For the measurements we used the white-light source and the VWF for selecting the desired wavelength. The cylindrical refractive lens was a plano–convex cylindrical lens made of BK7 material. The predicted dispersion of the cylindrical refractive lens is obtained from the dependence of its index of refraction on the wavelength, given by

$$n(\lambda) = \frac{b_1\lambda^2}{\lambda^2 - c_1} + \frac{b_2\lambda^2}{\lambda^2 - c_2} + \frac{b_3\lambda^2}{\lambda^2 - c_3},$$

where $b_1 = 1.0396$, $b_2 = 0.23179$, $b_3 = 1.01047$, $c_1 = 6.0007 \times 10^{-3}$, $c_2 = 2.00179 \times 10^{-2}$, and $c_3 = 1.0356 \times 10^2$, and the wavelength is given in micrometers. Using the thin-lens approximation, the refractive lens dispersion is given by

$$f_r(\lambda) = \frac{f_r(\lambda_0)[n(\lambda_0) - 1]}{n(\lambda) - 1}.$$

For the DOE the theoretical prediction for the dispersion, $f_d(\lambda)$, is given by Eq. (3). With the thin-lens approximation the theoretical dispersion relation of the combined diffractive–refractive lens with a gap d between them is given by

$$F(\lambda) = \frac{f_d(\lambda)[f_r(\lambda) - d]}{f_r(\lambda) + f_d(\lambda) - d}.$$

As evident, there is excellent agreement between the theoretical prediction and the experimental measurements of the dispersions of the refractive, diffractive, and combined optical elements (ADO). The dispersion of the ADO was measured to have a total focal

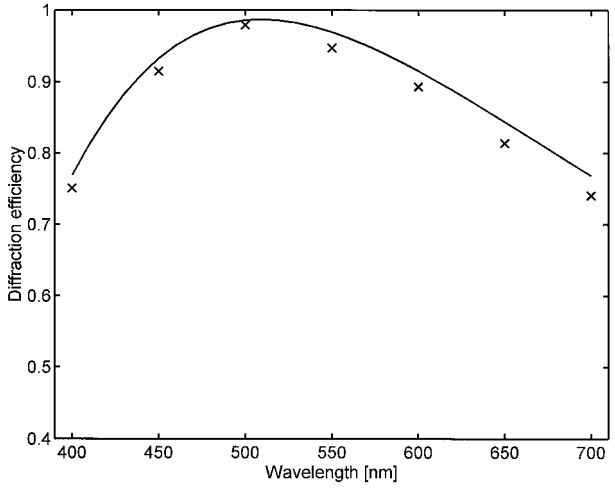

Fig. 4. Measured (crosses) and calculated (solid curve) diffraction efficiency of the DOE as a function of the wavelength.

length $F_0 = 326$ mm at λ_0, the focal depth of this combined lens was $\Delta F = 48$ mm, whereas the monochromatic focal depth (conventional) for $F_{\#} = 36$ was $\delta F \cong 2.7$ mm. Therefore the enlarging factor of the focal depth given by Eq. (6) is $M_o \cong 18$, which corresponds approximately to the predicted M_o using the Fresnel number of the diffractive optics as $N^{\mathrm{DOE}} \cong 36$ and $\Delta\lambda/\lambda_0 \cong 0.567$. The dispersion of our ADO was designed to be approximately linear (shown in Fig. 3); therefore the VWF in our experiments was the linear variable interference filter, SCHOTT VERIL S 60. The transmittance wavelength of the VWF varies along the 42-mm length of the filter, whereas the spectral width $\delta\lambda_f \cong 15$ nm, and the spectral band $\Delta\lambda \cong 300$ nm, yielding the VWF discrimination to be $M_f \cong 20$ [Eq. (8)], corresponding to the optimal consideration, $M_f^{\mathrm{opt}} \cong M_o$. The measured dispersion of the combined diffractive–refractive lens fits inside the linear VWF transmittance.[14]

The first-order diffraction efficiency for a multilevel binary DOE depends on the illumination wavelength λ. When we combine the results of Refs. 15 and16, the diffraction efficiency η_1 as a function of λ can be shown to be

$$\eta_1 = \left[\frac{\sin\left(\frac{\pi}{N}\right)}{\frac{\pi}{N}}\right]^2 \left[\frac{\sin\left(\pi\,\frac{\lambda_d - \lambda}{\lambda}\right)}{N \sin\left(\frac{\pi}{N}\,\frac{\lambda_d - \lambda}{\lambda}\right)}\right]^2, \qquad (11)$$

where N is the number of level and λ_d is the designed wavelength. In our experiments $N = 16$ levels. We choose $\lambda_d = 0.509$ μm so that the lowest diffraction efficiency in the visible spectrum (0.4–0.7 μm) is maximal. The measured and the theoretical predictions of the diffraction efficiency as a function of the wavelength are given in Fig. 4. As can be seen there is a good agreement between the predicted and the measured efficiencies, where >75% diffraction efficiency was obtained for the entire visible spectrum.

Two main configurations of the color-coded profilometer were investigated experimentally and theoretically. In the first configuration we used the rainbow light sheet directly without inserting the VWF, whereas in the latter a color-decoding technique was used with the VWF. Figure 5 shows measured sections of the imaged light-intensity distributions of the intersection between the rainbow light sheet and the flat object (a) without VWF and (b) with VWF. The improvement with the VWF is clearly evident. The intensity distribution without color decoding is significantly broad compared with the color-coding and decoding approach.

To test the experimental arrangement of the two configurations more quantitatively, we performed a series of measurements on a flat object, placed at an angle so as to include the entire focal range in the measurements. First, we measured the intensity

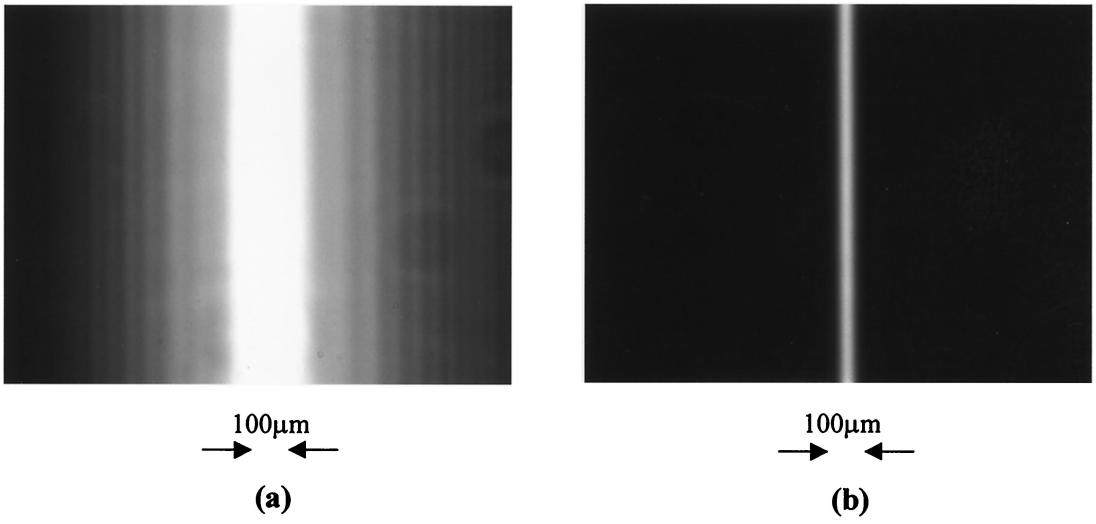

Fig. 5. Measured sections of the imaged light-intensity distributions of the intersection between the rainbow light sheet and a flat object: (a) without VWF and (b) with VWF.

cross-section distributions of the reflected light at three different locations along the focal range at the beginning of the focal range, $z = 299$ mm; the middle of the focal range, $z = 323$ mm; and at the end of the focal range, $z = 347$ mm. These measured intensity distributions were then compared with calculated intensity distributions. The predicted monochromatic intensity distributions were calculated by use of the Fresnel diffraction integral, given by

$$I(x_0, z, \lambda) = \frac{1}{(\lambda z)^2}\left|\int \exp[i\phi_L(x_1, \lambda)] \times \exp\left[i\,\frac{\pi}{\lambda z}\,(x_0 - x_1)^2\right] \mathrm{d}x_1\right|^2, \quad (12)$$

where the quadratic phase of the lens is $\phi_L(x_1, \lambda) = -\{(\pi x_1^2)/[\lambda F(\lambda)]\}$, with the total focal length of the combined diffractive–refractive elements $F(\lambda)$. The predicted polychromatic intensity distributions are calculated by

$$I_p(x_o, z) = \int S(\lambda) R^{\mathrm{VWF}}(\lambda) I(x_0, z, \lambda)\mathrm{d}\lambda, \quad (13)$$

where $S(\lambda)$ is the light-source spectrum and is the spectrum response of the VWF centered at the wavelength, which is focused at the calculated distance (focal length) z [note that $R^{\mathrm{VWF}}(\lambda) = 1$, for optical arrangement without the VWF]. The measured and the calculated results are presented in Figs. 6 and 7. Figures 6(a) and 6(b) show the measured and the calculated intensity cross sections, respectively, without use of the VWF. Both the measurement and the calculation reveal a broad undesirable background illumination combined with a small and narrow peak. Surprisingly, the calculations predict that the narrow peak remains clearly detectable above the broad background even when the enlarging factor of the focal depth, M_o, is considerably large, (e.g., $M_o > 500$). This by itself represents a plane version of a nondiffracting beam, analogs to the circular Bessel beam[17] produced by Axicon.[11,18] Figures 7(a)–7(c) show the measured and the calculated intensity cross sections when a VWF is used. As evident, there is a good agreement between the calculated and the measured intensity cross sections. The narrowing of the intensity cross sections, because of the VWF, is clearly seen, indicating that near-perfect matching between the ADO and filter dispersions was indeed obtained. Moreover, these results show that a diffraction-limited linewidth of approximately $\Delta x \cong 20$ μm at FWHM is maintained throughout the focal range when the VWF is used.

The resolvable depth of the system given by Eq. (9) depends on the accuracy required for determining the center of the image light distribution. Therefore an important quality criterion is the ratio between the maximal value of the peak to that of the sidelobe value, also known as the peak-to-background ratio. The peak-to-background ratio provides a limit on the allowed noise level that can be introduced into the system. Higher noise levels

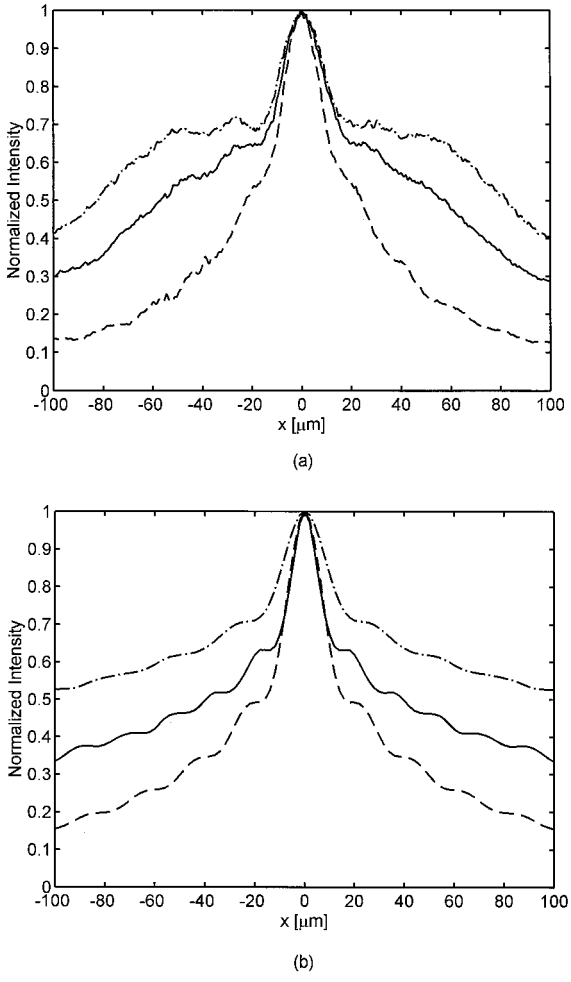

Fig. 6. Intensity cross sections at three positions along the focal range, without the VWF: (a) measured and (b) calculated. Dashed curve, $z = 299$ mm; solid curve, $z = 323$ mm; dotted–dashed curve, $z = 347$ mm.

significantly degrade the detected spot-size. For example, the results of Fig. 6 indicate that the peak-to-background ratio without a VWF is only ~1.5. In this case the noise level should be limited to 50% of the maximal background value. With VWF, however, the peak-to-background ratio improves significantly to ~15, and the permitted noise can reach values of 1500% of the maximal background value without significantly degrading its accuracy.

To determine the optical resolvable depth of our system with the VWF, it is necessary to scan an object with a known surface topography and compare the measured results with the given surface. This was done with a flat object (a high-quality laser mirror) placed at an angle. The measured profile of the flat object is shown in Fig. 8. For this measurement we used a 12-bit digital-cooled CCD camera, 1280 × 1024 pixels (Sensicam, PCO Computer Optics GmbH) and the centroid (center of gravity) algorithm to detect the center of the imaged line. The rms deviation of the measured result from the expected linear line was <40 nm. These results indicate that, for our

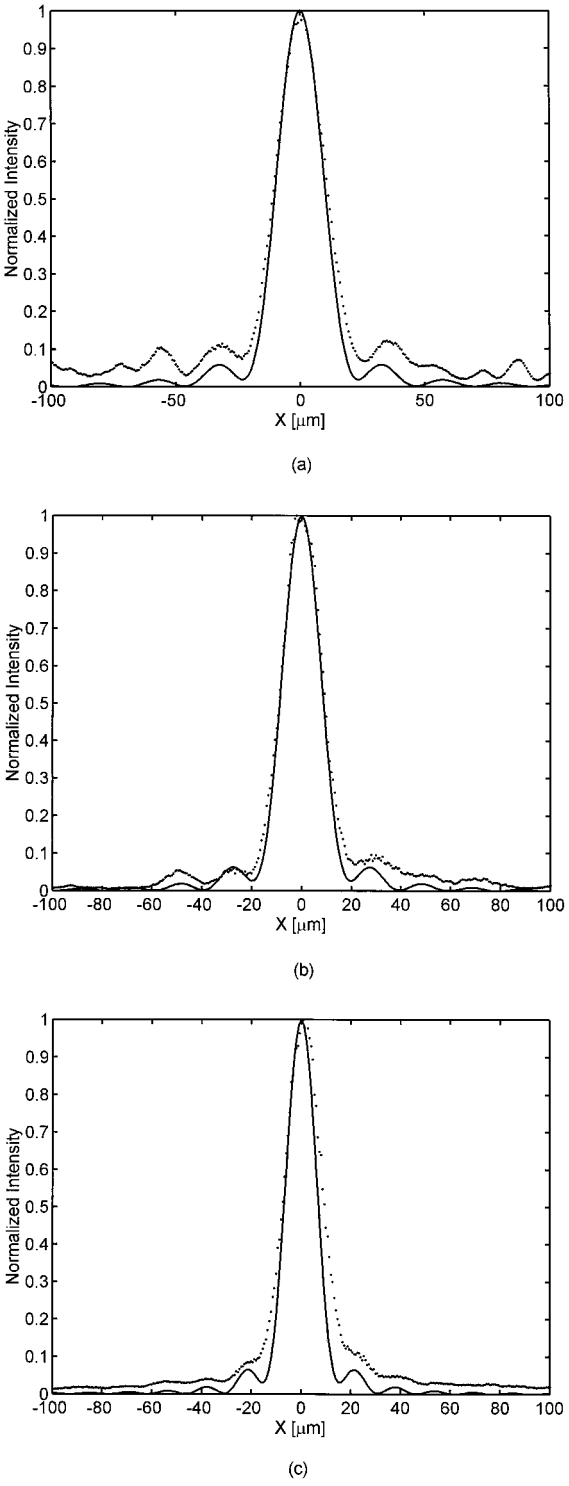

Fig. 7. Measured (dots) and calculated (solid curves) intensity cross sections at three positions along the focal range for (a) $z = 299$ mm, (b) $z = 323$ mm, (c) $z = 347$ mm.

lateral and depth resolutions of $\delta x \cong \delta z \cong 40$ nm ($\theta = \pi/2$), and for the extended depth measuring range of $\Delta F \cong 48$ mm, the number of NRD $\cong 1.2 \times 10^6$ [according to Eq. (10)] can be obtained. Note that, with a conventional incoherent triangulation approach (without color coding and decoding) and comparable noise level, the NRD would be only $\delta F/\delta z \approx 6 \times 10^4$. Also note that in conventional coherent (laser) triangulation systems the axial and the lateral resolutions are limited by speckle noise,[7–9] which often strongly reduces the NRD. However, in our approach with incoherent light, ~500-fold superresolution was obtained and, combined with an 18-fold increase of the focal range, yielded an extremely high NRD.

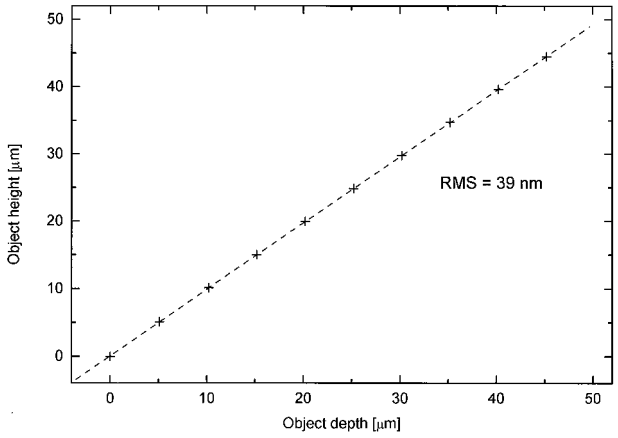

Fig. 8. Section of a measured profile of a flat object (pluses). Also shown is the expected linear object (dashed curve).

Our profilometer used real-time software for reading the data from the CCD camera and processing the center calculations. A single line cross section of the object's profile is obtained at video rates, so the time to complete a full 3-D scan of the object's surface was determined by the speed of the stepper motor.

4. Conclusions

We have presented what to our knowledge is a novel approach for rapidly determining the surface of 3-D objects. It is based on a color-coding arrangement that exploits polychromatic illumination and cylindrical, axially dispersing optics to increase the depth measuring range without any decrease in the lateral and axial resolutions. In a related approach a VWF, spectrally matched to the disperse illumination, is added to the observation system for color-decoding, to resolve completely the diffraction-limited spot size and shape through the entire depth measuring range. Our approach is also valid for even larger increase of the depth measuring range (e.g., $M_o > 500$) and for lenses with a small f-number, but more elaborate aberration-correction design for the axially dispersing optics will be needed. The main advantage of our approach over the conventional triangulation ones is that it exploits the additional degrees of freedom provided by the multiwavelength illumination in conjunction with the spatial data. This is in contrast to previous color-coding schemes[19] that use only the wavelength information instead of the spatial information, resulting in relatively poor discrimination ability.

This research was supported by the fund for the promotion of research at the Technion-Israel Institute of Technology.

References

1. T. Asakura, ed., *International Trends in Optics and Photonics ICO IV*: *Part VI, Optical Metrology*, Vol. 74 of Springer Series in Optical Sciences (Springer, New York, 1999), pp. 281–355.
2. E. Hasman, N. Davidson, and A. A. Friesem, "Multifunctional holographic elements for surface measurements," Opt. Eng. **31,** 363–368 (1992).
3. C. W. Tsai, C. H. Lee, and J. Wang, "Deconvolution of local surface response from topography in nanometer profilometry with a dual-scan method," Opt. Lett. **24,** 1732–1734 (1999).
4. M. Rioux, "Laser range finder based on synchronized scanners," Appl. Opt. **23,** 3837–3844 (1984).
5. D. W. Manthey, K. N. Knapp II, and D. Lee, "Calibration of a laser range-finding coordinate-measuring machine," Opt. Eng. **33,** 3372–3380 (1994).
6. J. A. Cox, "Point-source location using hexagonal arrays," Opt. Eng. **26,** 69–74 (1987).
7. R. G. Dorsch, G. Häusler, and J. M. Herrmann, "Laser triangulation: fundamental uncertainty in distance measurement," Appl. Opt. **33,** 1306–1314 (1994).
8. R. Baribeau and M. Rioux, "Centroid fluctuations of speckled targets," Appl. Opt. **30,** 3752–3755 (1991).
9. R. Baribeau and M. Rioux, "Influence of speckle on laser range finders," Appl. Opt. **30,** 2873–2878 (1991).
10. G. Bickel, G. Häusler, and M. Maul, "Triangulation with expended range of depth," Opt. Eng. **24,** 975–977 (1985).
11. N. Davidson, A. A. Friesem, and E. Hasman, "Efficient formation of non-diffracting beams with uniform intensity along the propagation direction," Opt. Commun. **88,** 326–330 (1992).
12. N. Davidson, A. A. Friesem, and E. Hasman, "Holographic axilens: high resolution and long focal depth," Opt. Lett. **16,** 523–525 (1991).
13. G. Häusler and W. Heckel, "Light sectioning with large depth and high resolution," Appl. Opt. **27,** 5165–5169 (1988).
14. E. Hasman, S. Keren, N. Davidson, and A. A. Friesem, "Three-dimensional optical metrology with color-coded extended depth of focus," Opt. Lett. **24,** 439–441 (1999).
15. E. Hasman, N. Davidson, and A. A. Friesem, "Efficient multilevel phase holograms for CO_2 lasers," Opt. Lett. **16,** 423–425 (1991).
16. N. Davidson, R. Duer, A. A. Friesem, and E. Hasman, "Blazed holographic gratings for polychromatic and multidirectional incidence light," J. Opt. Soc. Am. A **9,** 1196–1199 (1992).
17. J. Durnin, J. J. Miceli, Jr., and J. H. Eberly, "Diffraction-free beams," Phys. Rev. Lett. **58,** 1499–1501 (1987).
18. A. Vasara, J. Turunen, and A. T. Friberg, "Realization of general nondiffracting beams with computer-generated holograms," J. Opt. Soc. Am. A **6,** 1748–1754 (1989).
19. D. Mendlovic, "Three-dimensional imaging sensing based on a zone-plate array," Opt. Commun. **95,** 26–32 (1993).